Design of a CMOS image sensor pixel with embedded polysilicon nano-grating for near-infrared imaging enhancement

Elie Cobo, Sébastien Massenot, Alexandre Le Roch, Franck Corbière, Vincent Goiffon, Pierre Magnan, Jean-Luc Pelouard

Design of a CMOS image sensor pixel with embedded poly-silicon nano-grating for near-infrared imaging enhancement

ELIE COBO[1,*], SÉBASTIEN MASSENOT[1], ALEXANDRE LE ROCH[1], FRANCK CORBIÈRE[1], VINCENT GOIFFON[1], PIERRE MAGNAN[1], AND JEAN-LUC PELOUARD[2]

[1] *Institut Supérieur de l'Aéronautique et de l'Espace, Université de Toulouse, Toulouse, France*
[2] *Université Paris-Saclay, CNRS, Centre de Nanosciences et de Nanotechnologies (C2N), 91120 Palaiseau, France*
[*] *Corresponding author: elie.cobo@isae-supaero.fr*

CMOS (Complementary Metal-Oxide Semiconductor) image sensor sensitivity in the near-infrared spectrum is limited by the absorption length in silicon. To deal with that limitation, we evaluate the implementation of a polysilicon nano-grating inside a pixel, at the transistor gate level of a 90 nm standard CMOS process, through opto-electrical simulations. The studied pixel structure involves a polysilicon nano-grating, designed with the fabrication layer of the transistor gate, which does not require any modifications in the process flow. The diffraction effect of the nano-grating increases the length of the light path in the photosensitive area and thus increases the photoelectric conversion efficiency. The nano-grating is integrated in combination with deep trench isolations in order to reduce crosstalk between pixels. Coupled optical and electrical simulations report 33 % external quantum efficiency improvement and 7 % crosstalk reduction at 850 nm.

1. INTRODUCTION

Near-Infrared (NIR) spectrum detection has found several applications for imaging and machine vision. Multi-spectral camera using together color and NIR detection allow machine vision enhancement for portraying, shadow removal, vein detection and some industrial applications such as fruit and vegetable sorting, food inspection, tiles inspection[1–3]. Facial identification is a typical embedded function in smartphone using NIR detection[4] and applications as LIDAR based systems[5], Driver Assistance Systems[6], guidance systems[7] or security camera need the ability to imaging at low light level with a specific illumination sources commonly at 850 nm or 940 nm. NIR detection can also be useful in other contexts, such as plant tissue analysis[8] or medical imaging[9, 10]. Considering the growing demand of near-infrared imaging, the sensitivity of CMOS Image Sensor (CIS) for wavelength between 800 and 1100 nm has become a paramount consideration.

The CIS market is mainly driven by silicon based CIS for visible application. However, silicon is poorly absorbent in the NIR spectrum and represents a limiting parameter for affordable and scalable NIR detection for mass market. Moreover, CIS foundries use thin optically active layers, obtaining better performances for visible imaging but resulting with a drastic fall down of their performances for wavelength above 650 nm[11–13]. A typical active layer thickness is between 3 μm and 5 μm whereas, at a wavelength of 850 nm, the penetration depth after which the light is absorbed by 63% is over 18 μm in silicon. To be efficient, NIR detection with silicon needs significantly thicker photosensitive layer than what standard CIS fabrication usually allows. Therefore, some studies have investigated a detector with a thicker active layer in silicon[14, 15], making the photosensitive layer going deeper in the silicon with high resistivity epitaxial layer[16, 17] or by applying a negative voltage at the back of the photodiode[12] . Unfortunately, these solutions require processes adaptation differing from more conventional silicon based CIS. Consequently, NIR silicon based CIS require investment in equipment and process variation, impacting the production cost. Another enhancement method is about to extend the effective light path length inside the active layer with diffractive structures.

Backside illuminated CIS with pyramid structures has been extensively studied[18–21]. In addition, the principle of high absorption by a structure combining plasmonic diffraction and the use of metallic trenches has been demonstrated[22]. In the same idea, photodiodes with micro-structured holes have been designed and fabricated[23], the holes structure is used as photon-traps to improve the NIR detection of a single photodiode large of 30 μm. More recently, a single micro-hole structure per pixel

has been optically investigated for a silicon based CIS[24] showing a drastic increase on the optical efficiency through simulations and needing a specific etching step.

This work is focused on FrontSide Illuminated (FSI) devices and presents a solution for a NIR enhanced imaging sensor that does not need adding any supplementary steps in the process flow of a standard CIS fabrication. To doing this, the implementation of a poly-silicon nano-grating, designed from the layer of fabrication of the transistors gate, has been studied. In the same way, poly-silicon nano-gratings have already been implemented as reflectors[25–27] or color filters[28], it makes use of the transistor gate layer to design a nano-grating in order to reflect light or to be wavelength selective. In this paper, it is designed to diffract light inside the epitaxial layer and so enlarge the light path inside the photo-active region. The main advantage of this design is that it allows the use of the lithography and the etching steps of the transistors' gate fabrication, resulting in no additional manufacturing costs.

In addition, the use of Deep Trench Isolation[29, 30] (DTI) technology helps the diffracted light to be confined within the pixel avoiding it to spill over to the adjacent pixels, which it is named crosstalk and degrade image quality. FSI silicon based CIS with implemented nano-grating is investigated and designed by optical and electrical simulations, using LUMERICAL software, to enhance NIR detection at a wavelength of 850 nm. FSI CIS are relevant in applications where resolution and pixel size are not significant for primary interest, allowing to achieve high dynamic range and low cost fabrication. Optical and electrical coupling enables to calculate the total number of collected photogenerated carriers by the detector, whereas optical simulations alone calculate only the number of absorbed photons which is less representative of the detector efficiency.

2. METHODOLOGY

A. Pixel design

Figure 1.a) is a schematic cross sectional view of an FSI CIS pixel (standard pixel) it is composed of a silicon substrate on which a Si-epitaxial layer is grown. The epitaxial layer is P doped (P^{-}epi) two orders of magnitude less than the substrate (P^{++}sub). An N doped region (N-well) is introduced in the epitaxial layer in order to create the PN junction. At the top of the device are oxide layers and metallizations used to connect pixels and lecture nodes. The color filter is a spectral selective layer used in most cases for color reconstitution (e.g : Red, Green and Blue color filters), the layer between the oxide stack and the color filter is a passivation layer made of silicon nitride and on top of the pixel, the micro-lens is there to concentrate the light on the PN junction area, enhancing the fill factor and it also allows avoiding light scattering by the metallizations[31]. As an image sensor is made up of a matrix of pixels, each pixel needs to be electrically isolated from each other, which is achieved by the use of Shallow Trench Isolation (STI), a trench in silicon filled with oxide in order to prevent electric current leakage between adjacent pixel. Fig. 1.b) is the schematic cross-sectional view of an FSI CIS pixel architecture with integrated Poly-Si nano-grating and Deep Trench Isolation (DTI). As illustrated, the grating diffracts light and DTI replaces standard isolation in order to confine diffracted light inside the photodiode.

Fig. 1.c) and d) show a schematic top view of respectively the standard pixel and the pixel with integrated nano-grating, there is the photodiode dedicated to light absorption and the lecture node allowing to initialize the photodiode, to select the wanted pixel and to read its information. In the lecture node area, one can see the Poly-Si layer used for the fabrication of the gates of transistors. This transistors layer lithography and etching steps are used for the fabrication of the nano-grating on top of the photodiode, which does not involve any additional manufacturing steps compared to the standard pixel. Only the mask for making the transistor gates has to be modified.

In the remainder of this paper results of 2D simulations will be presented allowing conclusion only on a 1D nano-grating.

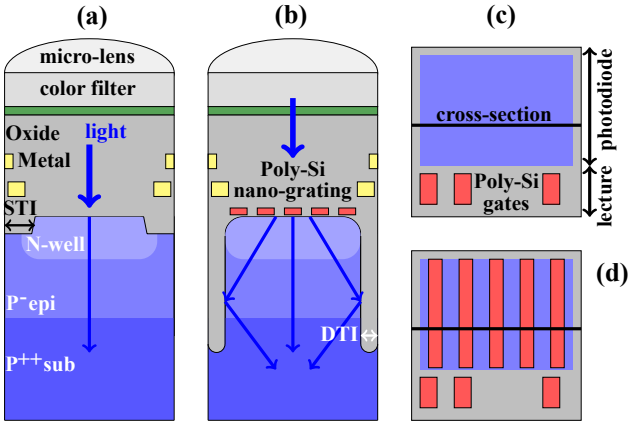

Fig. 1. A schematic cross-sectional (a) of a standard CMOS Image Sensor pixel and (b) of the new pixel architecture with poly-silicon nano-grating and Deep Trench Isolation. (c) and (d) the top view of respectively the standard and the new architecture pixel.

B. Figures of merit

The key properties of the pixel are its capability to collect as much of incident light as possible and its capability to avoid collecting light coming from neighbouring pixels. They are quantified by the External Quantum Efficiency (EQE) and the Crosstalk (CTK) that are used here as Figures Of Merit (FOM). The EQE corresponds to the ratio of the number of collected carriers (i.e. the number of electron-hole pairs) to the total amount of incident photons. Eq.1, shows that the EQE can be defined as the Internal Quantum Efficiency (IQE), which is the number of collected carriers over the absorbed photons, times the Optical Efficiency (OE), which is the number of absorbed photons over the number of incident photons. Therefore, the higher the EQE the brighter the image. The crosstalk occurs when a pixel collects carriers that should have not been collected by itself, but rather by the one of those next to it. CTK is, for a given pixel, the ratio of carriers collected which have been photo-created in a neighboring pixel as shown in Eq.2. It follows that the lower the CTK, the sharper the image, suppressing CTK gives better image contrast[32].

$$\underbrace{\frac{collected\ carriers}{incoming\ photons}}_{\text{EQE}} = \underbrace{\frac{collected\ carriers}{absorbed\ photons}}_{\text{IQE}} \times \underbrace{\frac{absorbed\ photons}{incoming\ photons}}_{\text{OE}} \times 100 \quad \textbf{(1)}$$

$$CTK = \frac{crosstalk\ collected\ carriers}{total\ collected\ carriers} \times 100 \quad \textbf{(2)}$$

A high EQE leads to a higher sensitivity, and a lower CTK leads to a higher image quality. These two parameters will be used to determine the enhancement of the new pixel design over the standard pixel design. In order to obtain the best image quality, the pixel design has to maximize the EQE and minimize the CTK. Most of the time, it will be a compromise between the two characteristics.

3. SIMULATIONS METHODOLOGY

A. Collected photogenerated-carriers

Three steps are needed for the simulation of EQE and CTK, the first one is the calculation of the optical excitation $E(\vec{r})$[33] (1 in Fig. 2), then comes the calculation of the absorption in the silicon leading to the photo-carriers generation function $G(\vec{r})$ (2 in Fig. 2). The last part is the calculation of the photo-carriers transport in the photodiode leading to the photo-carriers collection probability $P(\vec{r})$[34] (3 in Fig. 2). The first two parts involve optical simulation and the third part concern electrical simulation. The total amount of collected photo-carriers, $S_k(\vec{r})$, of the pixel k, is calculated by Eq.3 where $\vec{r}$ is the position vector. The integral is done over the photo-active region.

$$S_k = \int G(\vec{r})P(\vec{r})\,\mathrm{d}\vec{r} \tag{3}$$

The electrical calculation of $P(\vec{r})$ is done by considering the response to a generation rate point source located at $\vec{r}$. This impulse source is swept over all $\vec{r}$ in the simulation domain in order to achieve a complete map of $P(\vec{r})$. Therefore, $P(\vec{r})$ is calculated once for a specific junction architecture and then used for arbitrary optical inputs. The Block diagram in Fig. 2 summarizes the different calculation steps to obtain the total amount of collected photo-carriers for a specific illumination.

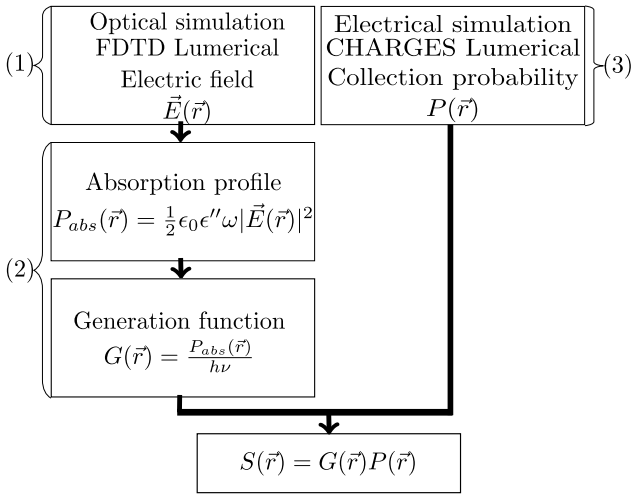

Fig. 2. Block diagram of the coupling between electrical and optical simulation

FDTD Lumerical software is used to solve the time-dependent Maxwell differential equations and calculate the electric field $\vec{E}(\vec{r})$ inside the photodiode for a specific optical excitation. From this electric field, the absorbed power $P_{abs}(\vec{r})$ is calculated, it gives the number of absorbed photons through Planck relation. The Lumerical software CHARGES is used to calculate the number of collected photo-carriers through the calcultation of carriers transport equations (drift and diffusion current) with Finite Element Method (FEM).

B. External Quantum Efficiency and Crosstalk calculation

In order to obtain the EQE and the CTK, two different simulations settings will be considered. Both of them involve three pixels to take into account the collection of carriers photo-generated in neighbouring pixels, named crosstalk. As it is shown in Fig. 1.c) the pixel is not symmetric, so the cross-section chosen for the 2D simulations (red line in the figure) is in the orientation that yields the most part of the crosstalk. Indeed, in the other orientation pixels are more distant from each other due to the lecture node, limiting the crosstalk.

The first setting is represented in Fig. 3.a) and the second setting is represented in Fig. 3.b). The two are similar, but one contains a filter transparent to the wavelength of calculation and in the other the central filter above the photo-diode of interest is opaque whereas filters above its adjacent pixels are transparent. For this filter layer, the real part of the refractive index is set at 1.5 and the imaginary part is set at 1.2 for the opaque one (transmitted intensity is more than 150 times lower than the incident one) and 0 for the transparent ones.

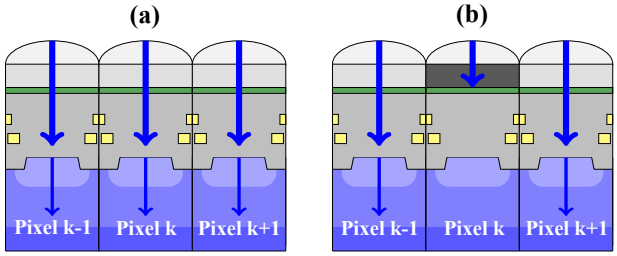

Fig. 3. Schematic cross-section of (a) the setting used for calculation of the total amount of collected photo-carrier and (b) the setting used for calculation of the crosstalked photo-carriers

Running optical and electrical simulations with settings of Fig. 3.a) allows the calculation of the total amount of collected photo-carriers by the pixel k, running them with the setting of Fig. 3.b) allows to obtain the number of collected photo-carriers by crosstalk. EQE is calculated from the setting of Fig. 3.a), though it contains all the photo-carriers collected by the pixels k including those resulting from crosstalk. The results are presented as the response of an unpolarized plane wave source which will be the average response of a parallel and a perpendicular polarized sources, as in Eq.4 where $|E|^2$ is the modulus square of the electric field results from an unpolarized source. $|E_s|^2$ (resp. $|E_p|^2$) is the modulus square of the electric field resulting from simulation in which the electric field is perpendicular (resp. parallel) to the plane of incidence.

$$|E|^2 = \frac{1}{2}|E_s|^2 + \frac{1}{2}|E_p|^2 \tag{4}$$

C. Parameters of the model

In table 1 are listed the geometric properties and the doping level of layers presented in Fig.1. The passivation layer is the intermediate layer of Si_3N_4 between the oxide stack and filters. The simulations are run considering a pixel width of 6 μm, which is a size that allows good dynamic range and with a DTI depth of 4 μm and an epitaxial layer thickness of 3 μm, typically optimized for low dark current and good EQE.

Regarding the optical properties of the different materials used, the silicon Si data are taken from Schinke et al.[35] for extinction coefficient values and from Vogt[36] for refractive

Table 1. Simulations parameters

layer	material	thickness	other
$P^{++}sub$	Si	27 μm	doping : 10^{18} cm^{-3}
$P^{-}epi$	Si	3 μm	doping : 10^{15} cm^{-3}
$N-well$	Si	800 nm	doping : 10^{18} cm^{-3}
Oxyde stack	SiO_2	3 μm	
STI / DTI	SiO_2	0.4 / 4 μm	width : 1 / 0.15 μm
passivation	Si_3N_4	200 nm	
filter	custom	1.05 μm	
micro-lens	SiO_2	1.5 μm	radius : 3 μm

index values. Fused silica SiO_2 and silicon nitrides Si_3N_4 data are taken from Phillip[37, 38]. Poly-silicon is considered to have the same optical properties as crystalline silicon[39] and metals are set as perfect electrical conductors.

4. NANO-GRATING OPTIMIZATION AND RESULTS

A complete optimization of the grating parameters is performed in order to find the best period and width of the grating at a 850 nm wavelength, used in typical NIR detection applications. First simulations are performed in order to calculate the references EQE and CTK so Fig. 4 and Fig. 5 are the simulations done for a pixel with standard oxide isolation and without nano-grating, cf. Fig. 1.a). The generation functions Fig. 4.a) and Fig. 5.a) multiplied by the collection probabilities Fig. 4.b) and Fig. 5.b) give the collected photo-carriers densities Fig. 4.c) and Fig. 5.c).

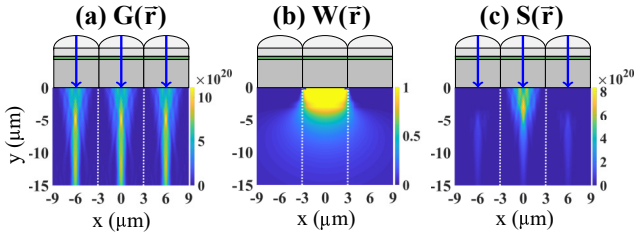

Fig. 4. Simulations for the EQE calculation (a) the generation function (carriers.m^{-2}.s^{-1}), (b) the probability of collection of the central pixel and (c) the density of photo-carriers collected by the central pixel (carriers.m^{-2}.s^{-1}).

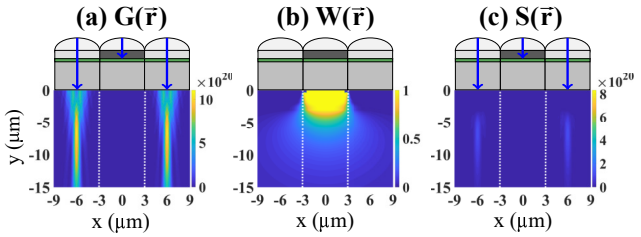

Fig. 5. Simulations for the CTK calculation (a) the generation function (carriers.m^{-2}.s^{-1}), (b) the probability of collection of the central pixel and (c) the density of photo-carriers collected by the central pixel (carriers.m^{-2}.s^{-1}).

The EQE calculated from Fig. 4 is equal to 26.6 %. The CTK is found equal to 20.4 % which is calculated from simulations of the setting Fig. 5, normalized by the amount of collected carriers calculated from Fig. 4.

A. Nano-grating parameters

In a 90 nm standard bulk CMOS process[40], the thickness of poly-silicium layer is 100 nm, the minimum structure width is 90 nm and the minimum spacing is 140 nm. This technology node allows fabrication of DTI[13] which are needed to reduce the cross-talking induced by the diffraction on the grating. The 1D grating parameters shown in Fig.6.a) are : the width (w), the spacing (s), the thickness (t) and the period (p). A thin layer of silicon nitride (Si_3N_4) is usually deposited during the fabrication process. There is an oxide layer of few nanometers under the Poly-Si gate, but it is not taken into account in the simulations due to its low impact and limited access to computing resources.

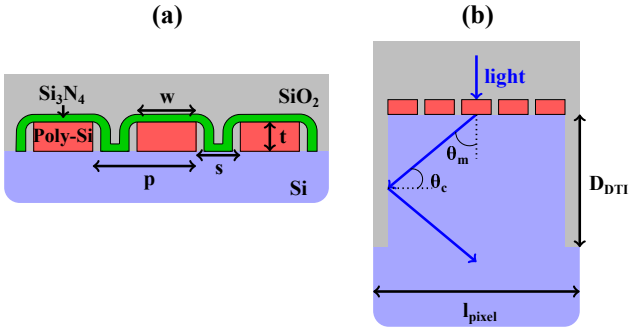

Fig. 6. a) A schematic poly-silicon nano-grating with indicated parameters : width (w), spacing (s), thickness (t) and period (p). b) The illustration of diffraction and total reflection.

Considering an incoming light at normal incidence θ_i, it is diffracted at the angles θ_m given by the Eq.5 where m is the diffraction order and p the period of the grating, Fig. 6.a) and Fig. 6.b).

$$\theta_m = \arcsin\left(\frac{m \times \lambda}{n_{Si} \times p}\right) \quad (5)$$

To stay in the conditions of the total internal reflection on the DTI-silicon interface, the diffracted angle θ_m must be smaller than the upper limit defined in Eq.6 so the angle θ_c in Fig. 6.b) is small enough to yield total reflection. Indeed, when the angle of reflection θ_m is too small, the total reflection condition is not satisfied, the light is not totally reflected so goes partially to the adjacent pixel and the image quality is degraded. In another hand, in order to be reflected by the DTI and because the depth of the DTI is finite, the diffracted angle must be greater than the lower limit defined in Eq.7, where l_{pixel} the size of the pixel and D_{DTI} the depth of the DTI. If not satisfied, the light goes beneath the DTI and illuminates the adjacent pixel.

$$\theta_m < \frac{\pi}{2} - \arcsin\left(\frac{n_{SiO_2}}{n_{Si}}\right) \quad (6)$$

$$\theta_m > \arctan\left(\frac{l_{pixel}}{2 \times D_{DTI}}\right) \quad (7)$$

Applying this to a wavelength of 850 nm, a DTI depth of 4 μm and a pixel size of 6 μm, results in an optimal period range between 255 and 389 nm, with $n_{SiO2} = 1.45$ and $n_{Si} = 3.64$. Here, we consider periods allowing only the diffraction of orders 0 and

+/- 1, because there are no configurations where the diffraction angles of orders +/-1 and +/-2 are both between the limit angles defined above.

B. Influence of the DTI width

The DTI width is dead space for imaging, the larger DTI width the smaller the photo-sensitive area. However, the DTI width must not be too small in order to efficiently reflect the diffracted light. Indeed, the reflected light could be coupled to the neighboring pixel by frustrated total internal reflection leading to loss a of energy reflected on the DTI. As illustrated Fig. 7.a), a part of the light goes through the trench by optical tunneling effect.

In order to optimize the DTI width, a simulation has been carried out considering the DTI depth infinite. The calculated CTK is presented in Fig. 7.b), the period of the nano-grating is set to 350 nm to obtain the first order of diffraction. The CTK is less than 1% for DTI widths greater than 250 nm.

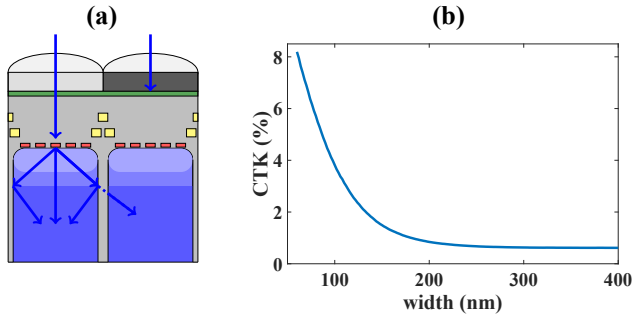

Fig. 7. (a) Illustration of frustrated total internal reflection inside a pixel (b) CTK as a function of DTI width considering the DTI depth infinite.

In the remainder of this paper, a DTI width of 150 nm will be considered[13], it represents a CTK of 1.6 % and corresponds to a trade-off between the size of the photo-sensitive area and the crosstalk.

C. Grating parametrization

The simulation methodology was applied for the proposed pixel structure (with a nano-grating) and with a DTI depth of 4 μm as illustrated by the Fig. 1.c). The simulations are conducted by stepping the period and the width of the nano-grating, looking for the optimization of the EQE without damaging the CTK compared to the standard structure. Fig. 8 shows the EQE and the CTK enhancement as a function of the period and the width of the nano-grating.

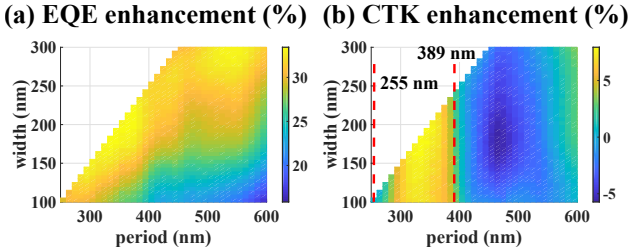

Fig. 8. a) EQE and b) CTK as function of the period and width parameters of the nano-grating, the limit $p > w + 140\ nm$ of the calculated values is due to the fabrication process.

The analytical result for the optimal period range (Eq. 5, 6, and 7), calculated previously, is also plotted in Fig. 8.b) (vertical dashed lines) and it shows that it is relatively well fitted to that of simulations. The analytical results are obtained considering an incident plane wave on the grating whereas in the simulations the plane wave is focused by the micro-lens before the grating, hence the slight differences observed between both models. The maximum EQE is reached for p = 360 nm and w = 195 nm, it is equal to 35.5 % which is an improvement of 33.5 % relatively to the standard pixel. It corresponds to a CTK of 19 % which is an enhancement of 6.9 % relatively to the standard pixel.

Fig. 9 shows the collection function of the photo-carriers $S(\vec{r})$ for the pixel k. It can be seen the diffraction induced by the grating and the reflection on the pixel side caused by the DTI.

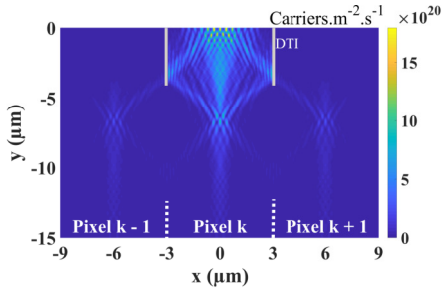

Fig. 9. The density of collected photo-carriers by the pixel k with a nano-grating (w = 195 nm ; p = 360 nm).

The new design proposal includes two modifications from the standard pixel architecture, the DTI that replaces the STI and the implemented grating on top of the photodiode. In order to highlight which of these modifications affect the EQE and the CTK, figure 10 shows results of four different designs: (1) the standard design that was calculated previously, (2) a pixel architecture with DTI alone, (3) a pixel with a grating but without DTI and (4) the architecture with both grating and DTI. The grating parameters are set to the optimal period and width values calculated earlier in this section.

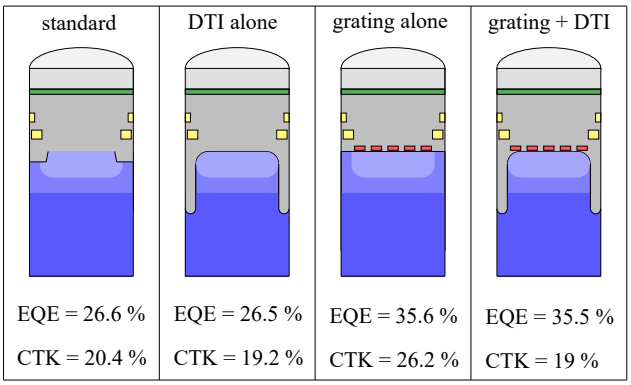

Fig. 10. EQE and CTK of a standard pixel, pixel with DTI alone, pixel with grating alone and pixel with both grating and DTI.

While the standard pixel and the pixel with DTI show the same EQE, the two designs that integrate grating show the same improvement in EQE. The grating implementation dominates the EQE increase. Besides, the grating architecture without DTI shows a drastic deterioration of the CTK, it is increased by

approximately 36.5 % whereas designs that contain DTI show a decrease in CTK from 20.4 % to 19.2 % and 19 %. The DTI implementation dominates the CTK decrease.

D. Polarimetric dependency

As the poly-silicon nano-grating is a 1D line, it generates a polarization dependent optical response. The EQE and the CTK diagrams for Transverse Magnetic (TM) and Transverse Electric (TE) polarizations are given in Fig. 11.a), b) and Fig. 12.a, b) respectively. The TE polarization (resp. TM) corresponds to an excitation with an electrical field perpendicular (resp. parallel) to the plane of incidence E_s (resp. E_p).

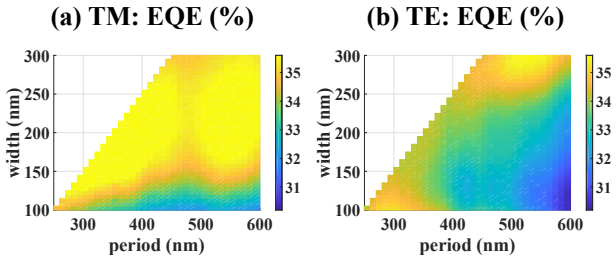

Fig. 11. EQE calculated with a source of (a) TM and (b) TE polarization.

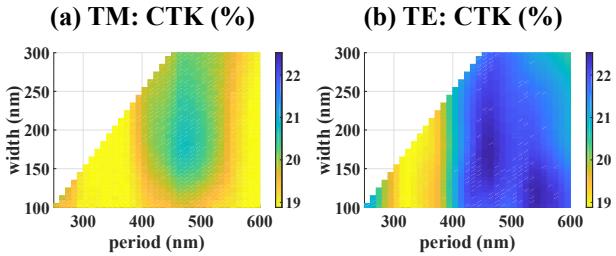

Fig. 12. CTK calculated with a source of (a) TM and (b) TE polarization.

For the optimal values of the period and the width obtained for a non-polarized light (p = 360 nm and w = 195 nm), EQE (resp. CTK) is equal to 34.1 % (resp. 19.1 %) in polarization TM and 36.9 % (resp. 18.8 %) in TE polarization. This weak dependence on polarization is attributed to the thin thickness of the grating (t = 100 nm) and could be made negligible by using a 2D symmetrical grating, which is intrinsically independent of polarization.

E. Spectral responses

The spectral response of a standard pixel and that of a pixel with nano-grating was calculated. The grating parameters come from the optimization at wavelength of 850 nm, presented in the previous section (p = 360 nm ; w = 195 nm). EQE and CTK are plotted Fig. 13.a) and b), as a function of wavelength, the dotted curve is for the standard pixel and the solid line is for the pixel with embedded grating.

The EQE is enhanced for wavelengths greater than 600 nm, and it can be noticed a drop at wavelengths smaller than 500 nm. This decrease is attributed to the optical losses due to absorption in the Poly-Si grating that become more significant in this wavelength range[39]. The CTK curves are globally similar, but the

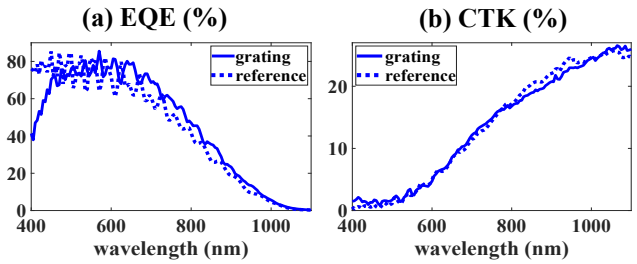

Fig. 13. a) EQE and b) CTK as function of the wavelength, dotted line is the reference standard pixel, solid line is the pixel with implemented nano-grating.

CTK for the pixel with embedded grating is significantly lower than the CTK of the reference between 800 nm and 1000 nm.

In summary, the proposed design allows for a combined improvement in EQE (increase) and CTK (decrease) for the wavelengths of application, meaning a higher image quality with better sensitivity and better contrast than standard pixels for wavelengths between 800 and 1000 nm.

F. Angular responses

The previous results are obtained with pixels illuminated by a plane wave source at normal incidence. These results already take into account the entire angular range provided by the micro-lens of the pixel. But in an imaging device, an upstream optical system focuses the light on the image sensor, meaning that the light comes with an angle of incidence on the pixel, even before the micro-lens. The angle seen by one pixel depends on its location in the pixel matrix and on the characteristics of the optical system. The pixels located on the edges of the matrix see a larger angle of incidence than the pixels in the center. So, for an imaging device to have homogeneous spatial image quality, it is important to minimize the EQE and CTK variations with the angle of incidence, shown in fig. 14.a) and b) respectively.

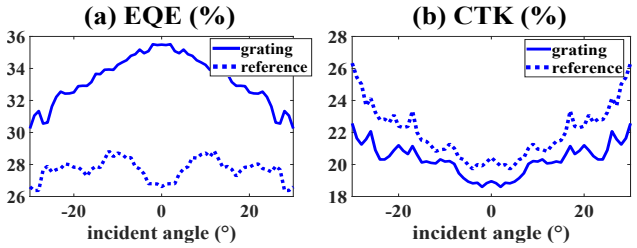

Fig. 14. a) EQE and b) CTK as function of the angle of incidence, dotted line is the reference standard pixel, solid line is the pixel with implemented nano-grating.

For all the angles of incidence studied here, the EQE and the CTK of the new architecture are improved compared to those of the standard pixel. The CTK variation trend of the grating pixel and the standard pixel is roughly the same for the two pixels. However, the EQE of the pixel with grating, drops from 35.5 % at normal incidence to 30.3 % at 30°, which is a larger variation than that of the standard pixel that stays in values of EQE between 26.6 % and 29 % for the same angular range. As it can be seen in figure 15.a), the transmission calculated at the interface SiO_2/Si just below the polysilicon nano-grating has the same trend than the EQE, meaning that the shape of the angular response depends is mainly defined by the transmission

of this interface. The introduction of a grating at the SiO2 / Si interface changes its optical response by two additional effects: more light penetrates into the silicon (anti-reflection effect) and the optical path in the silicon is increased (diffracted orders).

Even if the grating cannot be considered as a homogeneous medium (it diffracts in first orders), its optical behaviour gets close to that of an antireflective layer. For example, for a true antireflective layer between SiO_2 and Si, its ideal thickness would be $\lambda/\left(4\sqrt{n_{Si}n_{SiO2}}\right) \approx 92\ nm$ for $\lambda = 850\ nm$, a value very closed to the thickness of 100 nm of the polysilicon layer. As an illustration, Fig. 15.b) shows the EQE of the pixel as a function of the thickness of the poly-silicon grating. The maximum EQE is obtained for a thickness of 158 nm. This maximun depends of the nano-grating reflection and how this reflection influences the optical transmission of the all optical stack.

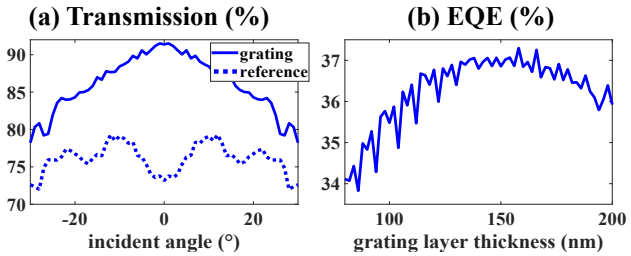

Fig. 15. a) Transmission at the interface $Si0_2/Si$ for the pixel with the integrated grating and the standard one b) EQE of the pixel with grating depending on the grating layer thickness.

As a conclusion for this section, the angular response of the pixel with the implemented grating shows that it over performes the standard pixel for a large angular range, making it relevant for imaging with large angle optics. However, the difference in quality between the edge and center pixels could be higher than that of imaging with a standard pixel.

5. INFLUENCE OF THE EPITAXIAL LAYER THICKNESS AND THE DEEP TRENCH ISOLATION DEPTH

A. Spectral study for a fixed deep trench isolation depth

A common and easiest way to enhance the NIR detection of a standard CIS is to thicken the epitaxial layer, allowing the carriers to be collected deeper in the silicon (life-time of carriers is longer in the epitaxy than in the substract). So far, in this paper, an epilayer thickness of 3 μm has been considered, designs with a 10 μm epitaxial layer will now be considered. All configurations studied in this part are shown in Fig 16.a). Standard E3 and grating E3 are the names of the designs previously studied. Standard E10 is for the standard pixel with an enlarged epitaxial layer of 10 μm and Grating E10 is a pixel with implemented nano-grating on an epitaxial layer of 10 μm. The DTI depth is kept at its previous value of 4 μm. Fig. 16.b) and Fig. 16.c) show results for the EQE and CTK for the four different pixels designs. All results are standardized by those of the standard E3 for ease of comparison.

It can be seen that the thickening of the epitaxial layer leads to an EQE enhancement, but also leads to a large deterioration of the CTK. If averaged values between 700 nm and 1100 nm are considered, the EQE of grating E3 is 20,4 % higher than the EQE of standard E3 whereas the EQE of standard E10 is 39.9 % higher than the one of standard E3. Then, the best EQE enhancement is for grating E10 (68.3 %). Considering the crosstalk, it can be seen that the CTK for grating E3 is better than the reference standard E3 (between 800 and 1000 nm). Grating E10 configuration is better than the standard E10. The 10 μm epitaxial layer degrades the CTK since the DTI depth of 4 μm considered here is not deep enough to be sufficiently efficient. A deeper DTI might give better results. This parameter will be theoretically investigated in the next part of this paper.

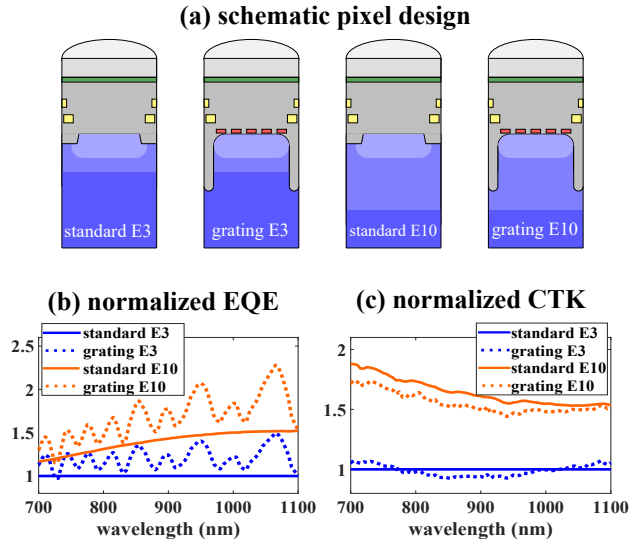

Fig. 16. a) schematic pixel design respectively for standard E3, grating E3, standard E10, grating E10. b) EQE and c) CTK as function of the wavelength.

At the wavelength of interest (850 nm), the EQE enhancement of "grating E3" structure is almost equivalent to that of "standard E10" its CTK is 60 % lower than that of "standard E10". So at 850 nm, the EQE of the design presented in this paper is equivalent to that of a pixel having an active layer more than three times thicker. While improving EQE by thickening the active layer leads to drastic deterioration of CTK, the design presented here improves both EQE and CTK.

B. Results for a variation of the epitaxial layer thickness and deep trench isolation depth at 850 nm

So far in this article, the depth of the DTI was fixed at a value of 4 μm, in this part, the influence of the DTI depth on EQE and CTK is studied for several epitaxial layers. Corresponding results are shown in Tab.2. For each combination of epitaxial thickness and DTI depth, the EQE and CTK are reported. These results are obtained for a wavelength of 850 nm and the grating parameters are set to p = 360 nm and w = 195 nm for all configurations. DTI depth of 6 μm and 8 μm will be studied, but as it is complicated to fabricate DTI deeper than 4 μm, the results are shown for theoretical knowledge, as a process development anticipation.

A first observation is that the CTK is deteriorated comparatively to the reference for DTI depths of 0 and 2 μm and is enhanced for values higher than 4 μm, whatever the thickness of the epitaxial layer. This corresponds to the minimum depth needed to have the first diffracted order of the nano-grating reflected by the DTI.

In addition, it can be seen that the EQE is almost independent of the DTI depth. Indeed, diffraction by nano-grating extends the light path in the silicon layer in a same proportion with and without DTI. When the DTI is not deep enough, light diffracted

Table 2. EQE and CTK calculation for different DTI and epitaxial layer thicknesses, results are presented for the grating parameters that optimize the EQE for a wavelength of 850 nm

DTI	FOM	Epitaxial thickness (μm)							
		3	4	5	6	7	8	9	10
reference	EQE	26.6%	29%	31%	32.7%	34.1%	35.1%	35.9%	36.6%
	CTK	20.4%	21%	23.8%	26.7%	29.2%	31%	32.4%	33.6%
0 μm	EQE	35.5%	38.6%	41.3%	43.4%	45%	46.5%	47.5%	48.4%
	CTK	26.6%	28%	30%	31.7%	32.9%	33.9%	34.6%	35.3%
2 μm	EQE	35.5%	38.6%	41.3%	43.5%	45.1%	46.4%	47.5%	48.4%
	CTK	25.6%	27%	29.1%	30.9%	32.2%	33.2%	34%	34.7%
4 μm	EQE	35.5%	38.7%	41.4%	43.6%	45.3%	46.6%	47.7%	48.5%
	CTK	19%	16.7%	21.3%	24.5%	27%	28.9%	30.2%	31.2%
6 μm	EQE	35.7%	38.7%	41.7%	44.5%	46.2%	47.5%	48.5%	49.3%
	CTK	15.8%	15%	14.1%	13.1%	21.7%	24.7%	26.7%	27.9%
8 μm	EQE	36%	39%	41.8%	44.5%	47.1%	49.6%	50.1%	50.7%
	CTK	12.7%	12.5%	12.3%	12.1%	11.8%	11.4%	22%	24.4%

by a nanograting propagates toward neighbour pixels and the number of photons collected by a pixel remains roughly the same because of the periodicity of the pixels.

DTI are efficient when their depth is greater than or equal to that of the epitaxial layer. For example, at DTI depth of 6 μm the CTK is 15.8 %, 15 %, 14.1 % and 13.1 % respectively for epitaxial thicknesses of 3 μm, 4 μm, 5 μm and 6 μm. Then the CTK jumps to 21.7 % for an epitaxial thickness of 7 μm and is growing higher with thicker epi-layer. An optimum is generally observed when the DTI depth equals the thickness of the epitaxial layer. Since the carrier life-time in the epitaxial layer is higher than that in the substrate (its doping level is much higher), most of the electrical cross-talk occurs in the epitaxial layer where the carriers likely to diffuse in neighboring pixels will be blocked by the DTI.

6. CONCLUSION

The near-infrared enhancement of the sensitivity of a standard frontside pixel of a CMOS image sensor with an integrated polysilicon nano-grating has been demonstrated through electro-optical numerical simulations. The pixel is designed so that it does not require any additional process steps compared to manufacturing a standard CMOS. It has been shown that the diffractive effect of a nano-grating combined together with deep trench isolation can lead to improved near-infrared detection without deteriorating the crosstalk compared to a standard pixel. The angular dependency of the pixel is slightly deteriorated by the nano-grating but is always more efficient for angles of incidence between 0 and 30°. At a wavelength of 850 nm, it has been shown that the near-infrared detection enhancement is about 33.5 % and the crosstalk is reduced by 6.9 %. The implementation of the nano-grating could lead to imaging in the near-infrared with better sensitivity and image contrast. The improvement in EQE provided by the nano-grating is equivalent to that of an active layer 3 times thicker but without the deterioration of CTK associated with this thickening. The best configurations are obtained with an epitaxial layer thickness equals to the DTI depth. For multi-spectral applications, each pixel could have its own grating parameters optimized for its operating wavelength.

FUNDING

Institut supérieur de l'aéronautique et de l'espace (ISAE).

DICLOSURES

The authors declare no conflicts of interest.

DATA AVAILABILITY

The data that support the findings of this study are available from the corresponding author upon reasonable request.

REFERENCES

1. Z. Chen, X. Wang, and R. Liang, "Rgb-nir multispectral camera," Opt. Express **22**, 4985–4994 (2014).
2. Y. Monno, H. Teranaka, K. Yoshizaki, M. Tanaka, and M. Okutomi, "Single-sensor rgb-nir imaging: High-quality system design and prototype implementation," IEEE Sensors J. **19**, 497–507 (2019).
3. D. Hertel, H. Marechal, D. A. Tefera, W. Fan, and R. Hicks, "A low-cost vis-nir true color night vision video system based on a wide dynamic range cmos imager," in *2009 IEEE Intelligent Vehicles Symposium,* (2009), pp. 273–278.
4. G. Zhao, X. Huang, M. Taini, S. Z. Li, and M. Pietikäinen, "Facial expression recognition from near-infrared videos," Image Vis. Comput. **29**, 607–619 (2011).
5. L. Mei and M. Brydegaard, "Atmospheric aerosol monitoring by an elastic scheimpflug lidar system," Opt. Express **23**, A1613–A1628 (2015).
6. J. Ge, Y. Luo, and G. Tei, "Real-time pedestrian detection and tracking at nighttime for driver-assistance systems," IEEE Transactions on Intell. Transp. Syst. **10**, 283–298 (2009).
7. G. Li, T. Yang, J. Li, X. Zhang, Z. Zhang, Z. Li, and Y. Zhang, "Infrared camera array system for air robot autolanding without gps," in *2016 IEEE 13th International Conference on Signal Processing (ICSP),* (2016), pp. 919–923.
8. S. Türker-Kaya and C. W. Huck, "A review of mid-infrared and near-infrared imaging: Principles, concepts and applications in plant tissue analysis," Molecules **22** (2017).
9. S. Luo, E. Zhang, Y. Su, T. Cheng, and C. Shi, "A review of nir dyes in cancer targeting and imaging," Biomaterials **32**, 7127–7138 (2011).

10. C. Yue, P. Liu, M. Zheng, P. Zhao, Y. Wang, Y. Ma, and L. Cai, "Ir-780 dye loaded tumor targeting theranostic nanoparticles for nir imaging and photothermal therapy," Biomaterials **34**, 6853–6861 (2013).
11. M. U. Pralle, J. E. Carey, H. Haddad, C. Vineis, J. Sickler, X. Li, J. Jiang, F. Sahebi, C. Palsule, and J. McKee, "IR CMOS: infrared enhanced silicon imaging," in *Infrared Technology and Applications XXXIX,* vol. 8704 B. F. Andresen, G. F. Fulop, C. M. Hanson, P. R. Norton, and P. Robert, eds., International Society for Optics and Photonics (SPIE, 2013), pp. 39 – 45.
12. S. Lauxtermann, J. Fisher, and M. McDougal, "A monolithic 640x512 CMOS imager with high-NIR sensitivity," in *Infrared Technology and Applications XL,* vol. 9070 B. F. Andresen, G. F. Fulop, C. M. Hanson, and P. R. Norton, eds., International Society for Optics and Photonics (SPIE, 2014), pp. 1 – 9.
13. C. Virmontois, C. Durnez, M. Estribeau, P. Cervantes, B. Avon, V. Goiffon, P. Magnan, A. Materne, and A. Bardoux, "Radiation effects in pinned photodiode cmos image sensors: Variation of epitaxial layer thickness," IEEE Transactions on Nucl. Sci. **64**, 38–44 (2017).
14. B. Dierickx and J. Bogaerts, "NIR-enhanced image sensor using multiple epitaxial layers," in *Sensors and Camera Systems for Scientific, Industrial, and Digital Photography Applications V,* vol. 5301 N. Sampat, R. J. Motta, and M. M. Blouke, eds., International Society for Optics and Photonics (SPIE, 2004), pp. 205 – 212.
15. V. C. Venezia, A. C.-W. Hsiung, W.-Z. Yang, Y. Zhang, C. Zhao, Z. Lin, and L. A. Grant, "Second generation small pixel technology using hybrid bond stacking," Sensors **18** (2018).
16. J. Lincelles, O. Marcelot, P. Magnan, O. Saint-Pé, and M. Bréart de Boisanger, "Enhanced near-infrared response cmos image sensors using high-resistivity substrate: Photodiodes design impact on performances," IEEE Transactions on Electron Devices **63**, 120–127 (2016).
17. X. Fang, Y. Xu, J. Yang, and K. Wu, "Analyses of pinned photodiodes with high resistivity epitaxial layer for indirect time-of-flight applications," IEEE Access **8**, 187575–187583 (2020).
18. Y. Hung, H. Su, C. Chun, J. Chen, C. Huang, and M. Cai, "Enhanced efficiency in backside-illuminated deep-n-well-assisted cmos photovoltaic devices," IEEE Electron Device Lett. **36**, 1169–1171 (2015).
19. I. Oshiyama, S. Yokogawa, H. Ikeda, Y. Ebiko, T. Hirano, S. Saito, T. Oinoue, Y. Hagimoto, and H. Iwamoto, "Near-infrared sensitivity enhancement of a back-illuminated complementary metal oxide semiconductor image sensor with a pyramid surface for diffraction structure," in *2017 IEEE International Electron Devices Meeting (IEDM),* (2017), pp. 16.4.1–16.4.4.
20. S. Yokogawa, I. Oshiyama, H. Ikeda, Y. Ebiko, T. Hirano, S. Saito, T. Oinoue, Y. Hagimoto, and H. Iwamoto, "IR sensitivity enhancement of CMOS Image Sensor with diffractive light trapping pixels," Sci. Reports **7** (2017).
21. C.-F. Han, J.-M. Chiou, and J.-F. Lin, "Deep trench isolation and inverted pyramid array structures used to enhance optical efficiency of photodiode in cmos image sensor via simulations," Sensors **20** (2020).
22. A. Ono, K. Hashimoto, and N. Teranishi, "Near-infrared sensitivity improvement by plasmonic diffraction for a silicon image sensor with deep trench isolation filled with highly reflective metal," Opt. Express **29**, 21313–21319 (2021).
23. Y. Gao, H. Cansizoglu, K. G. Polat, S. Ghandiparsi, A. Kaya, H. H. Mamtaz, A. S. Mayet, Y. Wang, X. Zhang, T. Yamada, E. P. Devine, A. F. Elrefaie, S.-Y. Wang, and M. S. Islam, "Photon-trapping microstructures enable high-speed high-efficiency silicon photodiodes," Nat. Photonics **11**, 301–308 (2017).
24. E. P. Devine, W. Qarony, A. Ahamed, A. S. Mayet, S. Ghandiparsi, C. Bartolo-Perez, A. F. Elrefaie, T. Yamada, S.-Y. Wang, and M. S. Islam, "Single microhole per pixel in cmos image sensors with enhanced optical sensitivity in near-infrared," IEEE Sensors J. **21**, 10556–10562 (2021).
25. Y. Hung, M. Hsieh, and J. Shih, "High-contrast polysilicon grating reflectors implemented in a standard bulk cmos line," IEEE Photonics Technol. Lett. **27**, 2170–2173 (2015).
26. Y. Hung, J. Chen, and C. Chun, "Improved performance in mirror-assisted back-contact cmos photovoltaic devices," IEEE Electron Device Lett. **36**, 478–480 (2015).
27. Y. Hung, C. Lu, J. Liao, and M. Hsieh, "Backside-illuminated cmos photodiodes with embedded polysilicon grating reflectors," IEEE Photonics Technol. Lett. **31**, 193–196 (2019).
28. J. Cong, D. Yan, J. Tang, W. Guo, and X. Mao, "Integrated color photodetectors in 40-nm standard cmos technology," IEEE Photonics Technol. Lett. **31**, 1979–1982 (2019).
29. Y. Kitamura, H. Aikawa, K. Kakehi, T. Yousyou, K. Eda, T. Minami, S. Uya, Y. Takegawa, H. Yamashita, Y. Kohyama, and T. Asami, "Suppression of crosstalk by using backside deep trench isolation for 1.12 μm backside illuminated cmos image sensor," in *2012 International Electron Devices Meeting,* (2012), pp. 24.2.1–24.2.4.
30. A. Tournier, F. Leverd, L. Favennec, C. Perrot, L. Pinzelli, M. Gatefait, N. Cherault, and D. Jeanjean, "Pixel-to-Pixel isolation by Deep Trench technology: Application to CMOS Image Sensor," in *2011 International Image Sensor Workshop (IISW),* .
31. T. Lopez, S. Massenot, M. Estribeau, P. Magnan, F. Pardo, and J.-L. Pelouard, "Integration of nanostructured planar diffractive lenses dedicated to near infrared detection for cmos image sensors," Opt. Express **24**, 8809–8823 (2016).
32. M. Estribeau and P. Magnan, "Pixel crosstalk and correlation with modulation transfer function of CMOS image sensor," in *Sensors and Camera Systems for Scientific and Industrial Applications VI,* vol. 5677 M. M. Blouke, ed., International Society for Optics and Photonics (SPIE, 2005), pp. 98 – 108.
33. F. Hirigoyen, A. Crocherie, J. M. Vaillant, and Y. Cazaux, "FDTD-based optical simulations methodology for CMOS image sensor pixels architecture and process optimization," in *Sensors, Cameras, and Systems for Industrial/Scientific Applications IX,* vol. 6816 M. M. Blouke and E. Bodegom, eds., International Society for Optics and Photonics (SPIE, 2008), pp. 65 – 76.
34. W. Gazeley, D. McGrath, and A. Imaging, "Quantum efficiency simulation using transport equations," in *2011 International Image Sensor Workshop (IISW),* .
35. C. Schinke, P. Christian Peest, J. Schmidt, R. Brendel, K. Bothe, M. R. Vogt, I. Kröger, S. Winter, A. Schirmacher, S. Lim, H. T. Nguyen, and D. MacDonald, "Uncertainty analysis for the coefficient of band-to-band absorption of crystalline silicon," AIP Adv. **5**, 067168 (2015). Publisher: American Institute of Physics.
36. M. R. Vogt, "Development of physical models for the simulation of optical properties of solar cell modules," Ph.D. thesis, Gottfried Wilhelm Leibniz Universität Hannover (2015).
37. H. R. Philipp, "Silicon dioxide (sio2) (glass)," in *Handbook of Optical Constants of Solids,* E. D. PALIK, ed. (Academic Press, Boston, 1985), pp. 749–763.
38. H. R. Philipp, "Optical properties of silicon nitride," J. The Electrochem. Soc. **120**, 295 (1973).
39. S. He and A. B. Sproul, "Optical properties of evaporated poly-Si thin-films on glass," Thin Solid Films **519**, 351–356 (2010).
40. T. Devoivre, M. Lunenborg, C. Julien, J. . Carrere, P. Ferreira, W. J. Toren, A. VandeGoor, P. Gayet, T. Berger, O. Hinsinger, P. Vannier, Y. Trouiller, Y. Rody, P. . Goirand, R. Palla, I. Thomas, F. Guyader, D. Roy, B. Borot, N. Planes, S. Naudet, F. Pico, D. Duca, F. Lalanne, D. Heslinga, and M. Haond, "Validated 90nm cmos technology platform with low-k copper interconnects for advanced system-on-chip (soc)," in *Proceedings of the 2002 IEEE International Workshop on Memory Technology, Design and Testing (MTDT2002),* (2002), pp. 157–162.